INORGANIC CHEMISTRY FRONTIERS

RESEARCH ARTICLE

View Article Online
View Journal | View Issue

Cite this: *Inorg. Chem. Front.*, 2023, **10**, 2626

Introducing anthracene and amino groups into Ln-OFs for the photoreduction of Cr(VI) without additional photosensitizers or cocatalysts†

Wenxiao Guo,‡[a] Shufang Wang,‡[a] Hongguo Hao,*[a] Xiangjin Kong,[a] Hui Yan,[a] Hongjie Zhu,[a] Yunwu Li,[a] Huawei Zhou,[a] Dichang Zhong*[b] and Fangna Dai[c]

The utilization of catalysts with high stability and activity for the photoreduction of Cr(VI) is desirable but has many challenges. Since metal–organic frameworks (MOFs) have unique versatilities and facile structural modulations, we fabricated a stable MOF as a highly efficient photocatalyst by incorporating chromophores into lanthanide MOFs for efficient Cr(VI) reduction. Subsequently, a novel two-dimensional (2D) layered structural Sm(III) MOF (namely **LCUH-100**, $[Sm_4(AAPA)_6(DMA)_2(H_2O)_4][DMA]_3[H_2O]_8$, $AAPA^{2-}$ = 5-[(anthracen-9-yl-methyl)-amino]-1,3-isophthalate, DMA = *N*,*N*′-dimethylacetamide) with *sql* topology symbol was constructed by incorporating dinuclear clusters, $\{Sm_2(COO)_6\}$ and $AAPA^{2-}$, which demonstrated excellent chemical and thermal stability, especially retaining its complete framework in aqueous solutions at a pH range of 2–12 for 24 h. Interestingly, **LCUH-100** could efficiently and rapidly photocatalyze the reduction of Cr(VI) to Cr(III) without additional photosensitizers or cocatalysts. In the photoreduction of Cr(VI), **LCUH-100** showed a high rate constant (k) of 0.186 min^{-1} and a high Cr(VI) reduction rate of 1.67 $mg_{Cr(VI)}\ g^{-1}_{cata}\ min^{-1}$ at pH 2. Furthermore, the photocatalyst **LCUH-100** could be reused for 5 cycles without any significant loss of catalytic activity. This work provides a new strategy for the exploitation of stable and efficient catalysts for the photocatalytic reduction of Cr(VI).

Received 15th January 2023,
Accepted 22nd March 2023

DOI: 10.1039/d3qi00102d

rsc.li/frontiers-inorganic

Introduction

Environmental issues are among the major issues facing the whole world today, including water contamination, which has caused wide public concern over the recent years.[1–4] Heavy metal ion pollution (*i.e.*, Cr(VI), Hg(II), and Fe(III)) is a significant global problem.[5–9] Especially, dichromate ($Cr_2O_7^{2-}$) ions are widely regarded as representative contaminant in water due to their high toxicity and carcinogenicity.[10–12] Therefore, the concentration of Cr(VI) in drinking water has been limited to below 0.05 mg L^{-1} by the World Health Organization.[13] Recently, many approaches have been exploited to efficiently adsorb and convert Cr(VI) into less toxic Cr ions.[14–16] In particular, the conversion of Cr(VI) into less toxic Cr(III) is regarded as a promising solution to alleviate the pollution problem. Since photocatalytic reduction is an eco-friendly method, solar-energy-driven $Cr_2O_7^{2-}$ ion reduction under the action of photocatalysts into Cr(III) has been extensively investigated.[17–19] Some typical inorganic photocatalysts with multifunctional characteristics have been reported by scientific researchers, such as TiO_2, α-Fe_2O_3, In_2S_3, and ZnO.[20–24] However, there are some shortcomings, such as the electron–hole pair recombination rate, fast agglomeration speed, and low solar energy utilization, which limit the efficiency of the above catalysts for Cr(VI) removal.[25–27] Therefore, the development of efficient photocatalysts to adsorb and convert Cr(VI) into a less toxic product Cr(III) is highly desired.

In recent years, diverse MOF catalysts have been exploited for Cr(VI) photoreduction.[28–34] Compared with three-dimensional (3D) MOFs, 2D MOFs have unique properties originating from their ultrathin thickness, large surface area, excellent optical transparency, and superior electrical and thermal conductivity, which facilitate a more efficient transport of photo-

[a]*Shandong Provincial Key Laboratory of Chemical Energy Storage and Novel Cell Technology, School of Pharmacy, School of Chemistry and Chemical Engineering, College of Materials Science and Engineering, and Dongchang College, Liaocheng University, Liaocheng 252059, China. E-mail: hhg207@126.com*
[b]*Institute for New Energy Materials and Low Carbon Technologies School of Materials Science and Engineering Tianjin University of Technology, Tianjin 300384, China. E-mail: dczhong@email.tjut.edu.cn*
[c]*College of Science, School of Materials Science and Engineering, China University of Petroleum (East China), Qingdao, Shandong 266580, China*

†Electronic supplementary information (ESI) available: Experimental, characterization and additional figures. CCDC 2170346. For ESI and crystallographic data in CIF or other electronic format see DOI: https://doi.org/10.1039/d3qi00102d

‡These authors are contributed equally to this work.

generated carriers from the interior to the surface active sites. Therefore, 2D MOFs are considered as more suitable photocatalyst candidates.[35–40] However, to the best of our knowledge, only a few articles have reported successful Cr(VI) photocatalytic reduction using 2D MOFs.[41,42] Meanwhile, chemists have found that 2D MOFs can be used as semiconductor materials, whereby the highest occupied molecular orbital (HOMO)–lowest unoccupied molecular orbital (LUMO) gap of the organic ligand in MOF systems is equal to the band gap of inorganic semiconductors, so it makes these photocatalysts possess the capabilities for fine-tuning and rational design at the molecular level.[43,44] For example, as the porphyrin unit is a typical photosensitizer, Ye's group successfully modified UiO-66 by introducing a porphyrin ring into the original UiO-66, and the photoreduction activity of the modified UiO-66 was much higher than that of the original UiO-66.[45] Wu's group found that the photoreduction activity of MIL-68 (In)-NH_2 was higher than the unmodified MIL-68(In), which indicated that adding amino groups in BDC^{2-} ligands could broaden the absorption edge to the visible region.[46] Therefore, an intense visible-light-absorption π-electron-rich aromatic unit and strong toxic anions adsorbent were integrated into one single MOF simultaneously to strongly improve the photoreduction capability toward Cr(VI). However, the photocatalysts obtained by the MOFs post-modification method do not have unambiguous structures, and their synthetic process is also more complicated. Based on the above considerations, we designed and obtained the 2D Sm-MOF **LCUH-100** using the ligand H_2AAPA containing anthracyclines and amino groups as photosensitizers, and this **LCUH-100** demonstrated excellent reactivity and good reproducibility for the reduction of Cr(VI) in water. As far as we know, this is the first example of a 2D lanthanide–organic frameworks (Ln-OFs) material among all the reported MOF-based photocatalysts for Cr(VI) photoreduction.

Herein, we rationally synthesized a stable Sm carboxylate MOF (**LCUH-100**) by using Sm(III) ions and the large conjugated dicarboxylate ligand H_2AAPA with amino groups (Scheme 1), which could broaden the absorption edge to the visible region. Notably, **LCUH-100** demonstrated excellent chemical and thermal stability, especially retaining its complete framework in aqueous solution at pH 2–12 for 24 h. Due to the introduction of highly photosensitive anthracene units and the cochromatic amino group, **LCUH-100** could achieve the complete conversion of Cr(VI) to Cr(III) within 60 min under visible-light irradiation without the need for any photosensitizer or cocatalyst. The significant photocatalytic activity of **LCUH-100** could be ascribed to its rich Lewis acidic Sm(III) sites, large conjugated dicarboxylate ligands, amino groups, and good charge-separation efficiency. Meanwhile, various factors affecting the reduction of Cr(VI), including the pH value of the reaction solution, the addition of a hole scavenger, and the reusability of the photocatalyst, were also studied in detail.

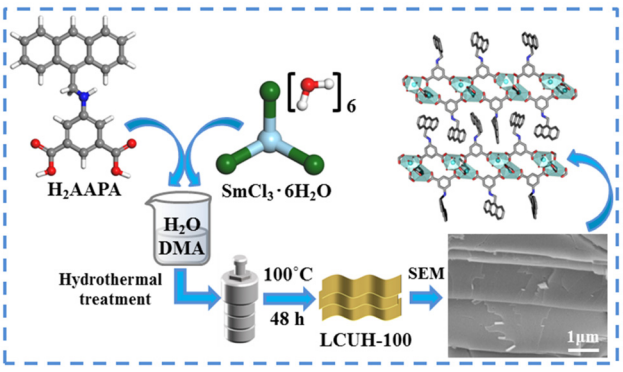

Scheme 1 Schematic illustration of the synthesis processes of **LCUH-100**.

Results and discussion

Structure and morphology description of LCUH-100

As shown in Table S1,† **LCUH-100** crystallized in a triclinic crystal system with space group $P\bar{1}$, displaying a two-dimensional (2D) framework based on the $AAPA^{2-}$ ligand and binuclear metallic $[Sm_2(COO)_6]$ cluster. In the asymmetric unit of **LCUH-100**, there are four independent Sm(III) ions, six deprotonated $AAPA^{2-}$ ligands, four coordinated H_2O molecules, and two coordinated organic solvent molecules (DMA), taking no account of the free solvent molecules. The four independent Sm(III) ions in the asymmetric unit can form two different binuclear metal clusters, namely $[Sm_2(COO)_6]^a$ and $[Sm_2(COO)_6]^b$. Four oxygen atoms (O5, O6, O16, O17) of one ligand link the binuclear clusters $[Sm_2(COO)_6]^a$ and $[Sm_2(COO)_6]^b$ (Fig. 1a). In the binuclear cluster $[Sm_2(COO)_6]^a$, Sm1 is a cation octa-coordinated by eight carboxylate oxygen atoms from five different deprotonated $AAPA^{2-}$ ligands, displaying a distorted dodecahedral geometry [Sm1–O5 = 2.32(8)

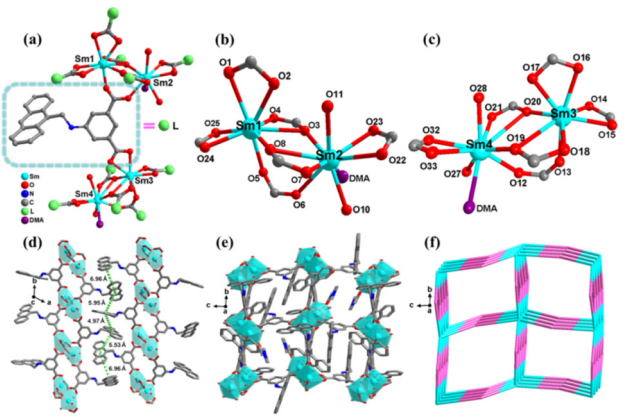

Fig. 1 (a) Simplified coordination environments of **LCUH-100** (green spheres represent H_2AAPA). Coordination structures of binuclear $[Sm_2(COO)_6]^a$ (b) and binuclear $[Sm_2(COO)_6]^b$ (c). (d) Lamellar structure of the 2D framework viewed from the *c* axis. (e) Reticular structure viewed from the *a* axis in **LCUH-100**. (f) Simplified topology structure of **LCUH-100**.

Å, Sm1–O8 = 2.34(8) Å, Sm1–O4 = 2.36(8) Å, Sm1–O2 = 2.41(10) Å, Table S2†]. The Sm2 center is nine-coordinated and composed of six carboxylate oxygen atoms from four different $AAPA^{2-}$, one oxygen atom from the coordinated DMA, and two oxygen atoms from two H_2O molecules [Sm2–O8 = 2.36(11) Å, Sm2–O3 = 2.41(8) Å, Sm2–O6 = 2.46(8) Å, Sm2–O7 = 2.46(8) Å, Table S2†]. The distance between Sm1 and Sm2 is 4.15 Å, and they are linked by two carboxylate oxygen atoms (O3 and O8) coming from two different $AAPA^{2-}$ ligands to form a binuclear metallic cluster $[Sm_2(COO)_6]^a$ (Fig. 1b).

In another binuclear cluster $[Sm_2(COO)_6]^b$, the Sm3 center is octa-coordinated by eight oxygen atoms from five different $AAPA^{2-}$ ligands, and displays a distorted dodecahedral geometry [Sm3–O13 = 2.35(7) Å, Sm3–O20 = 2.36(8) Å, Sm3–O18 = 2.39(7) Å, Sm3–O14^2 = 2.41(8) Å] (Table S2†). The Sm4 center is nine-coordinated by nine oxygen atoms and constituted by six carboxylate oxygen atoms from four different $AAPA^{2-}$ ligands, one oxygen atom from one DMA, and two oxygen atoms from two H_2O molecules [Sm4–O26 = 2.37(9) Å, Sm4–O19 = 2.41(8) Å, Sm4–O12 = 2.42(8) Å, Sm4–O21 = 2.48(8) Å. Table S2†]. The distance between Sm3 and Sm4 is 4.12 Å, and the adjacent two Sm(III) ions are connected by two carboxylate oxygen atoms (O19 and O20) from two different $AAPA^{2-}$ ligands (Fig. 1c). The adjacent binuclear metal clusters are linked through the deprotonated ligand $AAPA^{2-}$ and form 2D layered reticular structures (Fig. 1e). The distance between adjacent layers is in the range of 4.97–6.96 Å, so the adjacent 2D layers can be further connected to form 3D frameworks by the π···π stacking and hydrogen-bonding interactions (Fig. 1d). The framework of **LCUH-100** can be simplified to a 4-connected network with the *sql* topology of point symbol $\{4^4{\cdot}6^2\}$ by the topological analysis method (Fig. 1f). After removing guest molecules, the total solvent-accessible volume of **LCUH-100** was assessed to be 2043.2 Å^3, or 25.8% of the unit volume 7914.1 Å^3 calculated through PLATON.

The morphology and microstructure of the prepared **LCUH-100** were studied by field emission scanning electron microscopy (FESEM) and transmission electron microscopy (TEM), as shown in Fig. 2. Given the 2D crystal structure of **LCUH-100**, its FESEM images showed a typical layered appearance of 30–300 nm thickness (Fig. 2a). The morphology of **LCUH-100** was further observed by TEM (Fig. 2b), and the same 2D layered structure model was shown, which proved that we successfully prepared **LCUH-100** with a 2D layered structure.

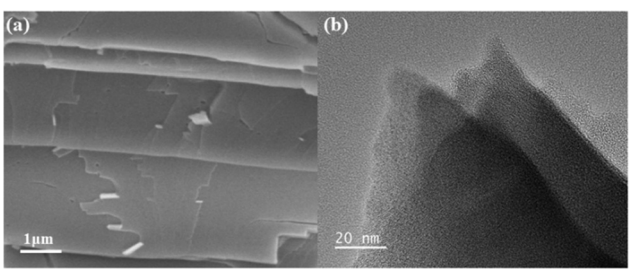

Fig. 2 FESEM (a) and TEM (b) images of **LCUH-100**.

Stability test

The powder X-ray diffraction (PXRD) patterns of **LCUH-100** indicated a good match between the simulated and as-synthesized **LCUH-100** in key positions, which confirmed the purity of the samples of **LCUH-100**. To inspect the chemical stability of **LCUH-100**, it was soaked in deionized water (pH 7), hydrochloric solution (pH = 2, 4, 6), and sodium hydroxide solution (pH = 8, 10, 12) at 298 K for 24 h, respectively. After the above soaking treatment, the PXRD patterns of the treated **LCUH-100** matched well with that of the simulated **LCUH-100** in key positions (Fig. 3a), indicating **LCUH-100** had excellent chemical stability, and ensure it can be used in further applications. Furthermore, the thermostability of MOFs is a significant element for their better application in industrial production. As shown in Fig. 3b, the thermogravimetric analysis indicated that **LCUH-100** had excellent thermostability and was thermally stable at 303 °C. Eight lattice water molecules were gradually lost in the range of 30–100 °C, corresponding to a 4.20% weight loss (*ca.* 4.15%). The further weight loss of 2.10% (*ca.* 2.08%) at 100–170 °C corresponded with the loss of four coordinated water molecules, and then at even higher temperature, the skeleton of **LCUH-100** began to collapse after 303 °C. In addition, **LCUH-100** was tested with variable temperature powders at 25–325 °C to further verify its stability, and the test results are displayed in the ESI, as shown in Fig. S2.†

Photocatalytic reduction of Cr(VI)

Photocatalytic properties. In the photocatalytic reaction, MOFs experience a process similar to that of traditional semiconductors. Note, the valence band (VB) and conduction band (CB) refer to the highest occupied molecular orbital (HOMO) and the lowest unoccupied molecular orbital (LUMO) in MOFs, respectively. The ultraviolet-visible-absorption band of **LCUH-100** was measured by ultraviolet–visible-light diffuse reflectance spectroscopy (UV–vis DRS). As displayed in Fig. 4a, the strong visible-light absorption and broad range absorption band (300–500 nm) make **LCUH-100** have potential application

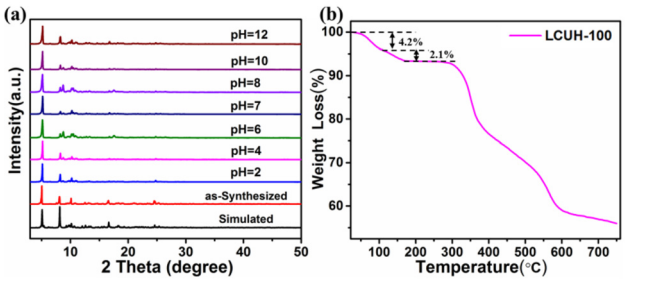

Fig. 3 (a) Simulated and synthetic PXRD patterns of **LCUH-100**, as well as the PXRD patterns of **LCUH-100** immersed in aqueous solutions of different pH values for 24 h; (b) thermogravimetric analysis (TGA) curves of **LCUH-100** measured under a N_2 atmosphere from 30 °C to 750 °C at a heating rate of 10 °C min^{-1}.

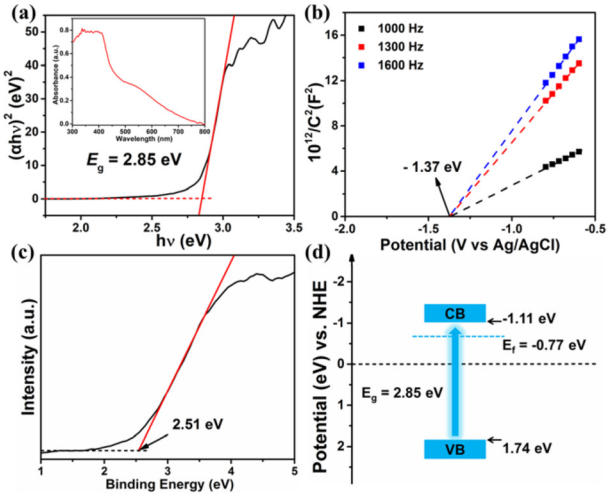

Fig. 4 (a) UV–vis spectra of **LCUH-100** and plot of $(\alpha h\nu)^2$ *versus* photon energy ($h\nu$) of **LCUH-100**. Typical Mott–Schottky plots (b) and XPS VB spectra (c) of **LCUH-100**. (d) Band structure diagram of **LCUH-100**.

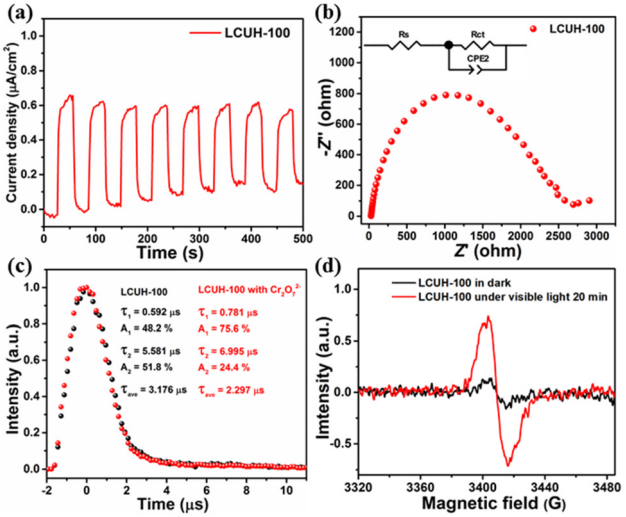

Fig. 5 Transient photocurrent responses (a), electrochemical impedance spectroscopy plot (b) of **LCUH-100**, time-resolved PL spectra of **LCUH-100** and **LCUH-100** containing $Cr_2O_7^{2-}$ suspensions (c), and of **LCUH-100**, (d) EPR analyses of **LCUH-100** before and after visible-light irradiation.

in visible-light photocatalysis.[47] The UV region (300–400 nm) absorption band was ascribed to the π···π* and n···π* transitions of the aromatic rings (An) and amino groups (–NH–) in the organic ligand $AAPA^{2-}$ of **LCUH-100**. While the visible region (400–550 nm) absorption band could be ascribed to the charge-transfer transition from the ligand $AAPA^{2-}$ to the $\{Sm_2\}$ cluster (LMCT).[48] The band-gap energy (E_g) of **LCUH-100** could be calculated based on the Kubelka–Munk equation: $\alpha h\nu = B(h\nu - E_g)^{1/2}$.[49] The E_g of **LCUH-100** was estimated to be about 2.85 eV by linear fitting the curve of $\alpha h\nu^2$ *versus* the photon energy ($h\nu$) (Fig. 4a). Therefore, the above DRS research endorsed the utilization of **LCUH-100** as a visible-light-active photocatalyst. To further investigate the band structure of **LCUH-100**, the semiconductor type and band potential (generally considered to be the Fermi level (E_f)) were determined by Mott–Schottky electrochemical tests. As shown in Fig. 4b, the slopes of the Mott–Schottky plots of **LCUH-100** (*i.e.*, 1000, 1300, and 1600 Hz) were all positive, indicating that **LCUH-100** can be regarded as an N-type characteristic material, and the E_f value was E_f (*vs.* Ag/AgCl) −1.37 eV, at pH 6.8. This could be converted into reversible hydrogen electrode (RHE) potential by the following formula: $E_{RHE} = E_{Ag/AgCl} + 0.198$ eV + 0.0592 pH, whereby the E_f value of **LCUH-100** was −0.77 eV (*vs.* RHE). Furthermore, the gap between E_f and VB obtained from the XPS VB spectra was 2.51 eV (*vs.* NHE) (Fig. 4c). The VB of **LCUH-100** was determined to be 1.74 eV (*vs.* NHE). Combined with the band-gap values obtained above, the CB of **LCUH-100** was calculated to be −1.11 eV (*vs.* NHE) (Table S5†), which was more negative than the Cr(VI)/Cr(III) potential (+0.51 eV, pH 6.8). Therefore, **LCUH-100** is a potential catalyst for the photocatalytic reduction of Cr(VI). As shown in Fig. 4d, based on the above analysis, the energy band diagram of photocatalyst **LCUH-100** was also schematically plotted.[43,50,51]

The separation efficiency of photogenerated charge carriers in **LCUH-100** was then investigated by transient photocurrent measurements, electrochemical impedance spectroscopy (EIS), and steady-state photoluminescence (steady-state PL). Fig. 5a shows the apparent photocurrent response (0.5 μA cm^{-2}) of the **LCUH-100** electrodes over on–off cycles of intermittent visible-light irradiation. This proves that **LCUH-100** was able to be stimulated to produce electron–hole pairs under visible irradiation.[52] The semicircle in the EIS spectra was due to the contribution from the charge-transfer resistance (R_{ct}) and constant phase element (CPE). The R_{ct} should result from the resistance at the interface between the photocatalyst/electrolyte interfaces. The corresponding equivalent circuit is shown in the inset of Fig. 5b. The radius of the EIS arc is related to the charge-transfer resistance of a photocatalyst, and a smaller radius of the EIS arc corresponds to a smaller resistance. According to the EIS results, the R_{ct} of **LCUH-100** was 2.7 kΩ, which was smaller than the R_{ct} of the photocatalysts reported in the literature. It is clear that **LCUH-100** had less charge-transfer resistance (for example, the R_{ct} of $H_2TCPPC(I^-)$ Meim-UiO-66 reported by Ye's group was 5.47 kΩ), which can make the photoexciton migration more effective.[10,15,16,23,43,45,50,51] This finding could be further confirmed by the steady-state PL spectrum (Fig. S3†). Interestingly, the PL intensity obtained over **LCUH-100** was much weaker than that of H_2AAPA, thus indicating the faster electron transfer of the photogenerated electrons and holes after forming the MOF material.[45,50,51]

Meanwhile, the time-resolved PL spectrum of **LCUH-100** is shown in Fig. 5c. The average recovery lifetime (τ) of **LCUH-100** was 3.176 μs. It is well known that prolongation of the exciton lifetime can provide more opportunities for photoinduced carriers to participate in surface-catalyzed reactions, thus improving the photocatalytic performance.[45,50] The electron-transfer process of the photocatalysts was further studied by electron

paramagnetic resonance (EPR), which was carried out in the dark and under visible-light irradiation, respectively (Fig. 5d). After 20 min visible-light irradiation, the EPR signal at about g = 2.002 was significantly enhanced, indicating that the photogenerated electrons transferred from the excited anthracene ring to the Sm–O cluster site.[43,45] However, when the other conditions were identical, no obvious signal was observed in the dark.

Photocatalytic reduction of Cr(VI) and its influencing factors. The excellent physical properties, strong visible-light adsorption and high electron–hole separation efficiency encouraged us to assess the feasibility of **LCUH-100** as a photocatalyst for Cr(VI) reduction. A negligible decrease in Cr(VI) was clearly observed in the presence of **LCUH-100** in the dark conditions, which indicated that the decline in the Cr(VI) concentration was not caused by adsorption. Whereas in the presence of light and the catalyst **LCUH-100**, the reduction process of Cr(VI) proceeded smoothly, and a significant decline in Cr(VI) concentration was observed, indicating that the reduction of Cr(VI) was caused by **LCUH-100** under visible-light irradiation. The Cr(VI) aqueous solution (50 ppm, 20 mL) could be 100% reduced within 60 min under the optimal conditions (pH 2, 3.0 mL EtOH) (Fig. 6a). As shown in Fig. 6b, the photoreduction of Cr(VI) followed a pseudo-first-order kinetics, and the reaction rate was calculated to be 0.1861 min^{-1} under the optimal conditions.[45] Compared with other reported MOF-related photocatalysts, the reduction efficiency of **LCUH-100** was at a high level for the reduction of Cr(VI) (Table 1).

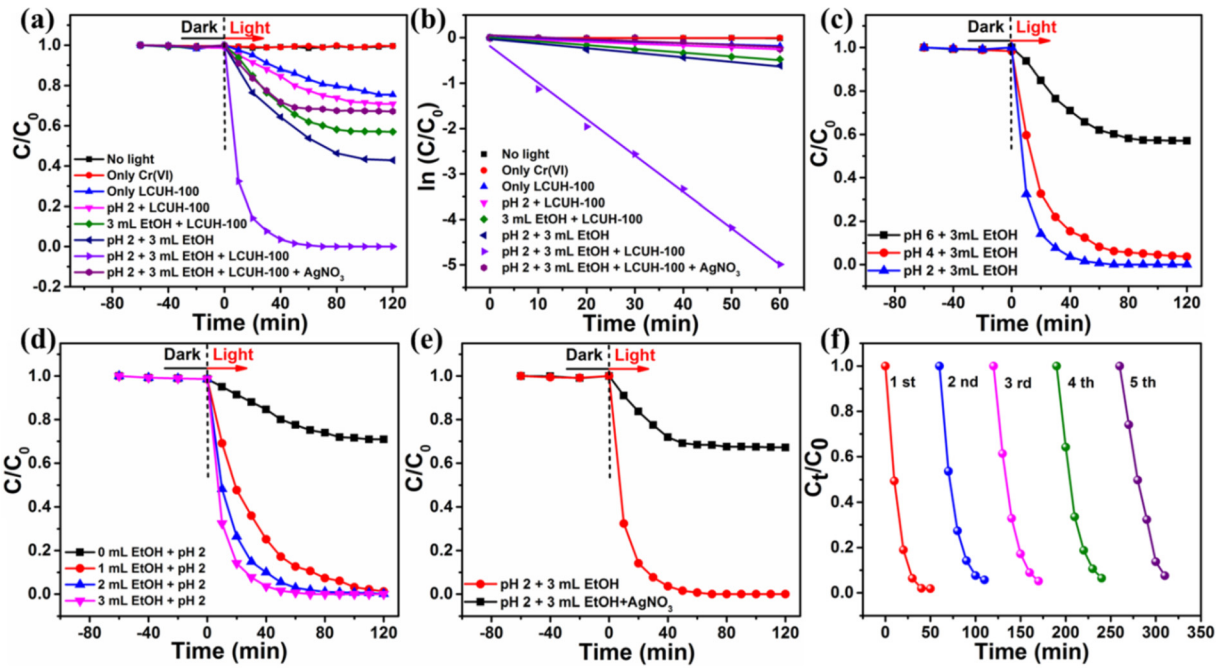

Fig. 6 Photocatalytic reduction of Cr(VI) to Cr(III): (a) under different conditions for Cr(VI) reduction over **LCUH-100** (pH 2, 3.0 mL of ethanol) and its pseudo-first-order kinetics curves (b); (c) with different pH in the presence of 3 mL ethanol; (d) with different amounts of EtOH at pH 2; (e) visible-light-driven photocatalytic Cr(VI) reduction of **LCUH-100** without (black curve) or with (red curve) the electron scavenger $AgNO_3$ (1 mg). (f) Cycling runs for the photocatalytic reduction of Cr(VI) over **LCUH-100**.

Table 1 Comparison of the photocatalytic reduction of Cr(VI) by different photocatalysts

Photocatalyst	C_{cata} (g L^{-1})	$V_{Cr(VI)}$ (mL); $C_{Cr(VI)}$ (ppm)	Reduction percentage; time (min)	Reduction rate ($mg_{Cr(VI)}$ g^{-1}_{cata} min^{-1})	k (min^{-1})	Light source	Ref.
In_2S_3@MIL-53(Fe)	0.60	50; 10	97%; 20	0.81	0.143	CEL-LAX 500 (300 W)	10
Cd-MOF	1.00	30; 20	95%; 180	0.11	—	LED lamp (40 W)	25
Cu(I)-MOF	0.38	40; 10	95%; 9	2.81	—	Xenon lamp (500 W)	42
Ru-UiO-bpy	0.25	40; 50	100%; 60	3.3	0.128	PLS-SXE300 (300 W)	43
NH_2-MIL-125-Ti	0.40	50; 48	91%; 60	1.82	—	Xenon lamp (500 W)	44
H_2TCPPC(I^-)Meim-UiO-66	0.25	40; 100	100%; 30	13.3	0.154	Xenon lamp (300 W)	45
MIL-68(In)-NH_2	1.00	40; 20	97%; 180	0.11	—	PLS-SXE300 (300 W)	46
Zn-MOF	1.00	40; 20	93%; 90	0.21	—	Xenon lamp (300 W)	47
Zr-MOF	0.25	40; 50	73%; 60	3.33	0.073	PLS-SXE300 (300 W)	49
LCUH-100	0.50	20; 50	100%; 60	1.67	0.186	CEL-LAX 500 (300 W)	This work

Moreover, the recycling tests indicated that **LCUH-100** had excellent recyclable stability, as identified by the PXRD patterns, IR spectra, and XPS spectra before and after the photoreduction of Cr(VI) (Fig. 6f and S4†). However, the rate of the photocatalytic reduction reaction was strongly affected by some factors, such as the pH, hole scavenger, and electron-capture agent.[49]

During the redox process, the pH value of the reaction solution had a great influence on the reduction rate, which was in agreement with that of other reported MOF catalysts.[10,44] Hence, the effect of pH on the photocatalytic performance was investigated under the concentration of 50 ppm $K_2Cr_2O_7$ solution (20 mL) and 10 mg of the catalyst **LCUH-100**. The reduction ratio increased rapidly from 41% to 100% with the pH decreasing from 6.0 to 2.0 (Fig. 6c). According to the surface zeta potential *versus* the pH of **LCUH-100**, the isoelectric point was about 2.56, which indicated that the photocatalyst surface was positive at the range of pH < 2.56 (Fig. S5†). Therefore, under the condition of pH 2, the positively charged photocatalyst **LCUH-100** was more likely to attract $Cr_2O_7^{2-}$ anions and accelerate the electron migration, thus promoting the photocatalytic activity. On the contrary, the significantly less reduction at higher pH (pH > 2.56) could be attributed to the highly anionic charged surface of the photocatalyst, which repelled the $Cr_2O_7^{2-}$ anions.

As is well known, the rate of photocatalytic reduction is greatly influenced by the presence of hole scavengers. The addition of a hole scavenger was thus used to trigger the reduction process, as it would react with the photoinduced holes. Herein, EtOH was investigated as a hole scavenger in the reaction, which could further promote the photocatalytic activities. As expected, as the amount of EtOH increased from 0 to 3 mL, the reduction rate increased rapidly from 23% to 100% (Fig. 6d). Therefore, EtOH could be beneficial to restrain the recombination of electrons and holes, which could afford sufficient electrons would be available for Cr(VI) reduction.[49]

The above experiments confirmed that the introduction of the hole (h^+)-scavenger EtOH could accelerate the reduction efficiency of Cr(VI). Herein, $AgNO_3$, as an electron scavenger, was introduced into the photocatalytic reduction process. As shown in Fig. 6e, the Cr(VI) reduction efficiency was obviously restrained by the solution of $AgNO_3$, indicating that the electron e^- had a dominant influence on the reduction process. The trapping of holes by EtOH may accelerate the migration of electrons e^- and make them fully participate in the reduction process, thereby finally improving the photocatalytic activity.[10]

Mechanism of photocatalytic Cr(VI) reduction

To investigate the electron-transfer process in the photocatalyst during visible-light irradiation, we then resorted to time-resolved PL spectroscopy, a robust tool to track photoexcited carriers. The τ of **LCUH-100** in Fig. 5c was 3.176 μs. After the addition of $Cr_2O_7^{2-}$, the average lifetime was reduced to 2.297 μs, indicating that the long-lived electrons generated by **LCUH-100** were easily transferred to $Cr_2O_7^{2-}$.[45,50] Meanwhile, EPR tests were performed to directly probe the photogenerated electrons in the reaction system. Here, 2,2,6,6-tetramethyl-l-piperidine-*N*-oxyl (TEMPO), as a typical spin label molecule, was utilized for capturing photogenerated electrons (e^-) on the surface of **LCUH-100** (Fig. 7a). The typical three signals of TEMPO with equal intensity were observed in the dark, but after visible-light irradiation for 20 min, the signal intensity dramatically declined. This could be ascribed to the TEMPO molecule being transformed into the corresponding hydroxylamine (TEMPOH) in aqueous system by trapping electrons.[53] The electrons e^- produced from the photoexcited **LCUH-100** were captured by TEMPO, which led to a weakening of the signal. Similarly, it was found that there was no obvious electronic signal after 20 min of visible-light irradiation when TEMPO molecules were replaced with $Cr_2O_7^{2-}$. The EPR data proved that the electrons e^- generated by photoexcited **LCUH-100** were captured by Cr(VI) and then reduced to Cr(III), and then $Cr_2O_7^{2-}$ ions were completely converted into Cr(III) ions under the irradiation of visible light, which was also proved by the XPS data of **LCUH-100**. As shown in Fig. 7b, the binding energies of Cr $2p_{3/2}$ and Cr $2p_{1/2}$ of Cr(III) corresponded to 578.0 and 587.3 eV, respectively.

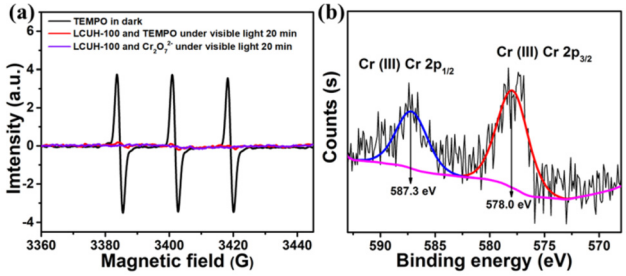

Fig. 7 (a) EPR signal of TEMPO in the dark, and TEMPO and $Cr_2O_7^{2-}$ radicals under visible light in aqueous dispersion of **LCUH-100** for 20 min; (b) XPS spectra of the recovered **LCUH-100** after the Cr(VI) reduction experiment.

According to the above experimental findings, a plausible mechanism is proposed for the reduction of Cr(VI) (Scheme 2).

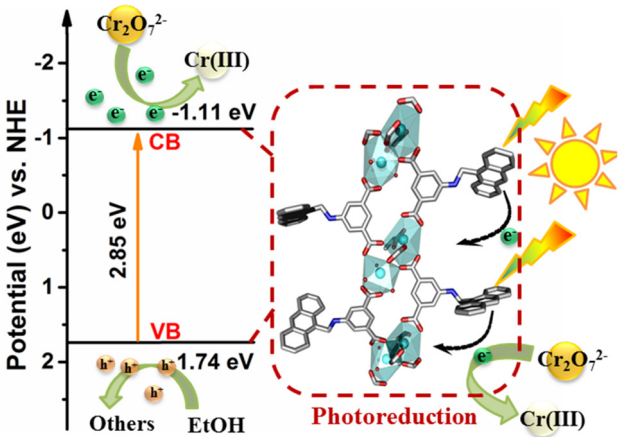

Scheme 2 Proposed mechanism for the photocatalytic reduction of aqueous Cr(VI).

In this process, the Sm–O clusters surrounded by H_2AAPA ligands in the framework of **LCUH-100** can behave as quantum dots, while the –NH– groups act as auxochromic groups, and the anthracene nucleus acts as an antennae absorbing light. Upon irradiation with visible light, the anthracene nucleus in **LCUH-100** strongly absorbs visible light and efficiently transfers the photogenerated electrons to the inorganic Sm–O clusters partly *via* ligand-to-metal charge transfer (LMCT) (eqn (1)). The electrons on the valence band leap into the conduction band and leave behind holes in the valence band, and then the electrons on CB are accepted by $Cr_2O_7^{2-}$ ions adsorbed on the metal sites (eqn (2)). Meanwhile, the photogenerated holes can get enough electrons from the hole scavenger EtOH adsorbed on the amine sites to oxidize EtOH into CO_2 and H_2O (eqn (3)).[43,46] Therefore, the redox process can be outlined as follows:

$$\text{Sm-MOF} + h\nu \rightarrow \text{Sm-MOF}\ (h^+ + e^-) \quad (1)$$

$$Cr_2O_7^{2-} + 14H^+ + 6e^- \rightarrow 2Cr^{3+} + 7H_2O \quad (2)$$

$$EtOH + h^+ \rightarrow CO_2 + H_2O + \text{Others.} \quad (3)$$

Conclusions

In summary, a 2D layered Sm-MOF, **LCUH-100**, with a good lattice and excellent stability was successfully prepared by a solvothermal method. The visible-light-absorption edge of **LCUH-100** could be extended to 550 nm by combining an anthracene group and amino group into the MOF framework, thus showing efficient Cr(VI) photocatalytic reduction performance. Remarkably, the photocatalytic reduction of Cr(VI) by **LCUH-100** did not require the aid of any photosensitizer or cocatalyst under visible-light irradiation, which is quite rare among reported MOF-based photocatalysts. **LCUH-100** showed a high rate constant (k) of 0.186 min^{-1} and a high Cr(VI) photoreduction rate of 1.67 $mg_{Cr(VI)}\ g^{-1}{}_{cata}\ min^{-1}$ for the photoreduction of Cr(VI), which are higher than most reported representative MOFs. In addition, **LCUH-100** demonstrated excellent photocatalytic reduction stability (5 recycling runs), making **LCUH-100** an outstanding candidate for the photocatalytic reduction of Cr(VI). This work provides a new method for the exploitation of stable and efficient catalysts for the photocatalytic reduction of Cr(VI).

Experimental section

Synthesis procedure

Synthesis of $\{[Sm_4(AAPA)_6(DMA)_2(H_2O)_4]\cdot DMA_3\cdot H_2O_8\}_n$ (LCUH-100). A mixture of $SmCl_3\cdot 6H_2O$ (36.48 mg, 0.1 mmol), 5-[(anthracen-9-yl methyl)-amino]-isophthalic acid (H_2AAPA) (13.7 mg, 0.05 mmol), dimethylacetamide (DMA, 3 mL), and deionized water (2.0 mL) was obtained with mechanical stirring for 30 min at room temperature. The mixture was transferred into a 10 mL Teflon-lined stainless steel vessel and heated at 100 °C for 48 h, and then cooled gradually to 298 K at a rate of 0.1 °C min^{-1}. Yellow rod-shaped crystals were collected with a 70% yield based on H_2AAPA. Anal. calcd for $C_{158}H_{159}N_{11}O_{41}Sm_4$ (3469.22): C 54.65, N 4.44, O 18.91, H 4.58. Found: C 54.20, N 4.74, O 18.85, H 4.68. FT-IR (KBr, cm^{-1}): 3403 (m), 3018 (w), 2980 (w), 1602 (s), 1425 (s), 1012 (w), 766 (s), 742 (s), 406 (s). The Fourier transform infrared spectra (FT-IR), as shown in Fig. S1.†

Photocatalytic reduction

The Cr(VI) photocatalytic reduction was achieved in a 100 mL quartz reactor at 298 K, and the reaction process was measured by UV–vis spectroscopy. The characteristic peak of $Cr_2O_7^{2-}$ was at 540 nm, and its absorbance gradually declined with time under visible-light irradiation. In a typical test, dichromate ($Cr_2O_7^{2-}$) was the main form of Cr(VI) under acidic solution, and dichromate potassium ($K_2Cr_2O_7$) was typically chosen as a representative Cr(VI) compound to achieve the photocatalytic reaction. Here, 10 mg catalyst **LCUH-100** and 20 mL $K_2Cr_2O_7$ aqueous solution (50 ppm) were uniformly dispersed into a 100 mL quartz reactor. The optimal pH value was 2.0 for the reaction solution, which could be adjusted with 0.2 mol L^{-1} H_2SO_4 dilute aqueous solution. First, the mixed solution was stirred vigorously in the dark for 60 min, which ensured **LCUH-100** could reach adsorption–desorption equilibrium for $K_2Cr_2O_7$. Second, the mixed solution was irradiated with a 300 W Xe lamp for 120 min. At regular intervals (10 min), 1.5 mL mixture was withdrawn from the 100 mL quartz reactor, and then filtered through a 0.22 μm hydrophilic membrane filter. At last, the filtered clear liquid was used for tracking tests by UV–vis spectroscopy using the previously reported diphenylcarbazide (DPC) method for the absorbance change of $Cr_2O_7^{2-}$. The above procedure was repeated for the rest of the mixture, and finally 13 group data points (including zero point) were successfully collected in 120 min.

Conflicts of interest

There are no conflicts to declare.

Acknowledgements

This work was supported by the National Natural Science Foundation of China (21401095, 21801107, 22178157), the Natural Science Foundation of Shandong Province (ZR2022MB010, ZR2019MB068, ZR2021QB123), Project of Shandong Province Higher Educational Science and Technology Program (KJ2018BZC043, J18KA113), the Liaocheng University Start-up Fund for Doctoral Scientific Research (318050104, 318052017), the Scientific Research Fund of Liaocheng University (318011913), the Youth Innovation Team of Shandong Colleges and Universities (2019KJC027, 2020KJC012), the Open Fund of Liaocheng University (2020CESNCTKL02), and the Shandong Students

Innovation and Entrepreneurship Training Program (319260210).

References

1 B. S. Rathi and P. S. Kumar, Application of adsorption process for effective removal of emerging contaminants from water and wastewater, *Environ. Pollut.*, 2021, **280**, 116995.
2 J. Theerthagiri, S. J. Lee, K. Karuppasamy, S. Arulmani, S. Veeralakshmi, M. Ashokkumar and M. Y. Choi, Application of advanced materials in sonophotocatalytic processes for the remediation of environmental pollutants, *J. Hazard. Mater.*, 2021, **412**, 125245.
3 Y. Wang, C. Kang, X. Li, Q. Hu and C. Wang, Ag NPs decorated C-TiO_2/$Cd_{0.5}Zn_{0.5}S$ Z-scheme heterojunction for simultaneous RhB degradation and Cr(VI) reduction, *Environ. Pollut.*, 2021, **286**, 117305.
4 B. Xue, L. Du, J. Jin, H. Meng and J. Mi, In situ growth of MIL-88A into polyacrylate and its application in highly efficient photocatalytic degradation of organic pollutants in water, *Appl. Surf. Sci.*, 2021, **564**, 150404.
5 J. Xiao, J. Liu, X. Gao, G. Ji, D. Wang and Z. Liu, A multichemosensor based on Zn-MOF: Ratio-dependent color transition detection of Hg(II) and highly sensitive sensor of Cr(VI), *Sens. Actuators, B*, 2018, **269**, 164–172.
6 H. Abdullah and D. H. Kuo, Facile Synthesis of n-type $(AgIn)_xZn_{2(1-x)}S_2$/p-type Ag_2S Nanocomposite for Visible Light Photocatalytic Reduction To Detoxify Hexavalent Chromium, *ACS Appl Mater Interfaces*, 2015, **7**(48), 26941–26951.
7 S. Das, S. Patnaik and K. M. Parida, Fabrication of a Au-loaded $CaFe_2O_4$/CoAl LDH p–n junction based architecture with stoichiometric H_2&O_2generation and Cr(VI) reduction under visible light, *Inorg. Chem. Front.*, 2019, **6**(1), 94–109.
8 P. Mahato, S. Saha, P. Das, H. Agarwalla and A. Das, An overview of the recent developments on Hg^{2+} recognition, *RSC Adv.*, 2014, **4**(68), 36140–36174.
9 D. Mallick, B. Biswal, M. Thirunavoukkarasu, R. Mohanty and B. Bag, Signalling probes appended with two rhodamine derivatives: inter-component preferences, Fe(iii)-ion selective fluorescence responses and bio-imaging in plant species, *New J. Chem.*, 2017, **41**(24), 15144–15156.
10 L. Luo, S. Dong, H. Cui, L. Sun and T. Huang, Indium sulfide deposited MIL-53(Fe) microrods: Efficient visible-light-driven photocatalytic reduction of hexavalent chromium, *J. Colloid Interface Sci.*, 2022, **606**, 1299–1310.
11 P. Kar, T. K. Maji, P. K. Sarkar, P. Lemmens and S. K. Pal, Development of a photo-catalytic converter for potential use in the detoxification of Cr(VI) metal in water from natural resources, *J. Mater. Chem. A*, 2018, **6**(8), 3674–3683.
12 M. Faisal, F. A. Harraz, A. E. Al-Salami, A. M. El-Toni, A. A. Almadiy, A. Khan, J. P. Labis, S. A. Al-Sayari and M. S. Al-Assiri, Enhanced photocatalytic reduction of Cr(VI) on silver nanoparticles modified mesoporous silicon under visible light, *J. Am. Ceram. Soc.*, 2019, **102**(9), 5071–5081.
13 R. A. Hamouda, N. E. El-Naggar, N. M. Doleib and A. A. Saddiq, Bioprocessing strategies for cost-effective simultaneous removal of chromium and malachite green by marine alga Enteromorpha intestinalis, *Sci. Rep.*, 2020, **10**(1), 13479.
14 G. Yuan, F. Li, K. Li, J. Liu, J. Li, S. Zhang, Q. Jia and H. Zhang, Research Progress on Photocatalytic Reduction of Cr(VI) in Polluted Water, *Bull. Chem. Soc. Jpn.*, 2021, **94**(4), 1142–1155.
15 D. Dai, J. Qiu, L. Zhang, H. Ma and J. Yao, Amino-functionalized Ti-metal-organic framework decorated BiOI sphere for simultaneous elimination of Cr(VI) and tetracycline, *J. Colloid Interface Sci.*, 2022, **607**(Pt 2), 933–941.
16 S. Prakash Tripathy, S. Subudhi, S. Das, M. Kumar Ghosh, M. Das, R. Acharya, R. Acharya and K. Parida, Hydrolytically stable citrate capped Fe_3O_4@UiO-66-NH_2 MOF: A hetero-structure composite with enhanced activity towards Cr(VI) adsorption and photocatalytic H_2 evolution, *J. Colloid Interface Sci.*, 2022, **606**(1), 353–366.
17 Y.-X. Li, Y.-C. Han and C.-C. Wang, Fabrication strategies and Cr(VI) elimination activities of the MOF-derivatives and their composites, *Chem. Eng. J.*, 2021, **405**.
18 V. Kumar, V. Singh, K.-H. Kim, E. E. Kwon and S. A. Younis, Metal-organic frameworks for photocatalytic detoxification of chromium and uranium in water, *Coord. Chem. Rev.*, 2021, **447**, 214148.
19 B. Valizadeh, T. N. Nguyen, S. Kampouri, D. T. Sun, M. D. Mensi, K. Stylianou, B. Smit and W. L. Queen, A novel integrated Cr(VI) adsorption–photoreduction system using MOF@polymer composite beads, *J. Mater. Chem. A*, 2020, **8**(19), 9629–9637.
20 Y.-J. Lee, C.-G. Lee, J.-K. Kang, S.-J. Park and P. J. J. Alvarez, Simple preparation method for Styrofoam–TiO_2 composites and their photocatalytic application for dye oxidation and Cr(VI) reduction in industrial wastewater, *Environ. Sci.: Water Res. Technol.*, 2021, **7**(1), 222–230.
21 A. Mohamed, T. A. Osman, M. S. Toprak, M. Muhammed, E. Yilmaz and A. Uheida, Visible light photocatalytic reduction of Cr(VI) by surface modified CNT/titanium dioxide composites nanofibers, *J. Mol. Catal. A: Chem.*, 2016, **424**, 45–53.
22 V. P. Viswanathan, A. N. Nayarassery, M. M. Xavier and S. Mathew, A 2D/1D heterojunction nanocomposite built from polymeric carbon nitride and MIL-88A(Fe) derived α-Fe_2O_3 for enhanced photocatalytic degradation of rhodamine B, *New J. Chem.*, 2022, **46**(19), 9064–9074.
23 C. Yang, R. Wang, W. Zhu, J. Wang, L. Zhang, T. Du, Z. Liu, L. Xie, J. Sun and J. Wang, Construction of In_2S_3@ZIF-8@$ZnIn_2S_4$ hierarchical nanoflower heterostructures to promote photocatalytic reduction activity, *Inorg. Chem. Front.*, 2022, **9**(1), 51–59.
24 B. Abebe and H. C. A. Murthy, Insights into ZnO-based doped porous nanocrystal frameworks, *RSC Adv.*, 2022, **12**(10), 5816–5833.

25 H. Kaur, R. Kumar, A. Kumar, V. Krishnan and R. R. Koner, Trifunctional metal-organic platform for environmental remediation: structural features with peripheral hydroxyl groups facilitate adsorption, degradation and reduction processes, *Dalton Trans.*, 2019, **48**(3), 915–927.
26 S. Mondal, S. Das and U. K. Gautam, Defect-rich, negatively-charged SnS_2 nanosheets for efficient photocatalytic Cr(VI) reduction and organic dye adsorption in water, *J. Colloid Interface Sci.*, 2021, **603**, 110–119.
27 C.-R. Chen, H.-Y. Zeng, S. Xu, J.-C. Shen, G. Hu, R.-L. Zhu, J.-Z. Du and Y.-X. Sun, Facile fabrication of CdS/ZnAlO heterojunction with enhanced photocatalytic activity for Cr(VI) reduction under visible light, *Appl. Clay Sci.*, 2018, **165**, 197–204.
28 H. C. Zhou and S. Kitagawa, Metal-organic frameworks (MOFs), *Chem. Soc. Rev.*, 2014, **43**(16), 5415–5418.
29 A. Schneemann, V. Bon, I. Schwedler, I. Senkovska, S. Kaskel and R. A. Fischer, Flexible metal-organic frameworks, *Chem. Soc. Rev.*, 2014, **43**(16), 6062–6096.
30 H. C. Zhou, J. R. Long and O. M. Yaghi, Introduction to metal-organic frameworks, *Chem. Rev.*, 2012, **112**(2), 673–674.
31 A. Pankajakshan, A. Ravarikkandy, B. P. Ratheesh, M. P. Maman and S. Mandal, Thiol decorated defective metal-organic frameworks embedded with palladium nanoparticles for efficient Cr(VI) reduction, *Inorg. Chem. Front.*, 2021, **8**(23), 5093–5099.
32 J. Qiu, X. Zhang, Y. Feng, X. Zhang, H. Wang and J. Yao, Modified metal-organic frameworks as photocatalysts, *Appl. Catal., B*, 2018, **231**, 317–342.
33 C.-C. Wang, X.-D. Du, J. Li, X.-X. Guo, P. Wang and J. Zhang, Photocatalytic Cr(VI) reduction in metal-organic frameworks: A mini-review, *Appl. Catal., B*, 2016, **193**, 198–216.
34 Y. Gu, Y. N. Wu, L. Li, W. Chen, F. Li and S. Kitagawa, Controllable Modular Growth of Hierarchical MOF-on-MOF Architectures, *Angew. Chem., Int. Ed.*, 2017, **56**(49), 15658–15662.
35 Y. Pan, R. Abazari, J. Yao and J. Gao, Recent progress in 2D metal-organic framework photocatalysts: synthesis, photocatalytic mechanism and applications, *J. Phys.: Energy*, 2021, **3**(3), 032010.
36 H. Kaur, S. Sinha, V. Krishnan and R. R. Koner, Photocatalytic Reduction and Recognition of Cr(VI): New Zn (II)-Based Metal-Organic Framework as Catalytic Surface, *Ind. Eng. Chem. Res.*, 2020, **59**(18), 8538–8550.
37 Z. W. Jiang, T. T. Zhao, S. J. Zhen, C. M. Li, Y. F. Li and C. Z. Huang, A 2D MOF-based artificial light-harvesting system with chloroplast bionic structure for photochemical catalysis, *J. Mater. Chem. A*, 2021, **9**(14), 9301–9306.
38 Z. Zhang, Y. Wang, B. Niu, B. Liu, J. Li and W. Duan, Ultrastable two-dimensional metal-organic frameworks for photocatalytic H_2 production, *Nanoscale*, 2022, **14**(19), 7146–7150.
39 J. Wang, J. Zhang, S. B. Peh, L. Zhai, Y. Ying, G. Liu, Y. Cheng and D. Zhao, Dimensional Impact of Metal–Organic Frameworks in Catalyzing Photoinduced Hydrogen Evolution and Cyanosilylation Reactions, *ACS Appl. Energy Mater.*, 2018, **2**(1), 298–304.
40 C. Tan, X. Cao, X. J. Wu, Q. He, J. Yang, X. Zhang, J. Chen, W. Zhao, S. Han, G. H. Nam, M. Sindoro and H. Zhang, Recent Advances in Ultrathin Two-Dimensional Nanomaterials, *Chem. Rev.*, 2017, **117**(9), 6225–6331.
41 Y. Xue, G. Zhao, R. Yang, F. Chu, J. Chen, L. Wang and X. Huang, 2D metal-organic framework-based materials for electrocatalytic, photocatalytic and thermocatalytic applications, *Nanoscale*, 2021, **13**(7), 3911–3936.
42 D. M. Chen, C. X. Sun, C. S. Liu and M. Du, Stable Layered Semiconductive Cu(I)-Organic Framework for Efficient Visible-Light-Driven Cr(VI) Reduction and H_2 Evolution, *Inorg. Chem.*, 2018, **57**(13), 7975–7981.
43 H.-Q. Zheng, X.-H. He, Y.-N. Zeng, W.-H. Qiu, J. Chen, G.-J. Cao, R.-G. Lin, Z.-J. Lin and B. Chen, Boosting the photoreduction activity of Cr(VI) in metal–organic frameworks by photosensitiser incorporation and framework ionization, *J. Mater. Chem. A*, 2020, **8**(33), 17219–17228.
44 H. Wang, X. Yuan, Y. Wu, G. Zeng, X. Chen, L. Leng, Z. Wu, L. Jiang and H. Li, Facile synthesis of amino-functionalized titanium metal-organic frameworks and their superior visible-light photocatalytic activity for Cr(VI) reduction, *J. Hazard. Mater.*, 2015, **286**, 187–194.
45 X.-S. Wang, C.-H. Chen, F. Ichihara, M. Oshikiri, J. Liang, L. Li, Y. Li, H. Song, S. Wang, T. Zhang, Y.-B. Huang, R. Cao and J. Ye, Integration of adsorption and photosensitivity capabilities into a cationic multivariate metal-organic framework for enhanced visible-light photoreduction reaction, *Appl. Catal., B*, 2019, **253**, 323–330.
46 R. Liang, L. Shen, F. Jing, W. Wu, N. Qin, R. Lin and L. Wu, NH 2 -mediated indium metal–organic framework as a novel visible-light-driven photocatalyst for reduction of the aqueous Cr(VI), *Appl. Catal., B*, 2015, **162**, 245–251.
47 X.-D. Du, X.-H. Yi, P. Wang, W. Zheng, J. Deng and C.-C. Wang, Robust photocatalytic reduction of Cr(VI) on UiO-66-NH_2(Zr/Hf) metal-organic framework membrane under sunlight irradiation, *Chem. Eng. J.*, 2019, **356**, 393–399.
48 R. Liang, F. Jing, G. Yan and L. Wu, Synthesis of CdS-decorated MIL-68(Fe) nanocomposites: Efficient and stable visible light photocatalysts for the selective reduction of 4-nitroaniline to p-phenylenediamine in water, *Appl. Catal., B*, 2017, **218**, 452–459.
49 X. Wang, Y. Zhang, Z. Shi, T. Lu, Q. Wang and B. Li, Multifunctional Zr-MOF Based on Bisimidazole Tetracarboxylic Acid for pH Sensing and Photoreduction of Cr(VI), *ACS Appl. Mater. Interfaces*, 2021, **13**(45), 54217–54226.
50 D. Liu, C. Li, C. Zhao, Q. Zhao, T. Niu, L. Pan, P. Xu, F. Zhang, W. Wu and T. Ni, Facile synthesis of three-dimensional hollow porous carbon doped polymeric carbon nitride with highly efficient photocatalytic performance, *Chem. Eng. J.*, 2022, **438**, 135623.

51 Y. Liu, Y. Liu, Y. Xu, Q. He, R. Yin, P. Sun and X. Dong, Phenanthroline bridging graphitic carbon nitride framework and Fe(II) ions to promote transfer of photogenerated electrons for selective photocatalytic reduction of Nitrophenols, *J. Colloid Interface Sci.*, 2022, **608**, 2088–2099.
52 H.-Y. Zhang, Y. Yang, C.-C. Li, H.-L. Tang, F.-M. Zhang, G.-L. Zhang and H. Yan, A new strategy for constructing covalently connected MOF@COF core–shell heterostructures for enhanced photocatalytic hydrogen evolution, *J. Mater. Chem. A*, 2021, **9**(31), 16743–16750.
53 C. Zhao, Z. Chen, J. Xu, Q. Liu, H. Xu, H. Tang, G. Li, Y. Jiang, F. Qu, Z. Lin and X. Yang, Probing supramolecular assembly and charge carrier dynamics toward enhanced photocatalytic hydrogen evolution in 2D graphitic carbon nitride nanosheets, *Appl. Catal., B*, 2019, **256**, 117867.